Progress In Electromagnetics Research M, Vol. 111, 173–183, 2022

Refractive Index Sensing Performances of a Mid-Infrared Asymmetric MZI Based on Suspended GaAs Waveguides

Fang Wang[1, 3], Shoudao Ma[1], Tao Ma[1, 3, *], Xu Wang[1, 3], Kun Yu[2], and Lei Li[1]

Abstract—A novel mid-infrared (MIR) biochemistry sensor using two suspended GaAs waveguides based on an asymmetric Mach-Zender Interferometer (MZI) is proposed. The propagation properties and refractive index (RI) sensing performances of MZI are investigated by the finite element method (FEM). The simulation results show that the maximum waveguide sensitivities (S_{wg}) of the TE and TM modes in the suspended GaAs waveguide are ~ 1.2 and ~ 1.0. This design of the GaAs waveguide using the suspension structure is to enhance the interaction between the vanishing field and measured material. The RI sensitivity of the asymmetric MZI structure increases with the length of the sensing arm, which can reach 854.5 nm/RIU with a Q of 208.2 after parameter optimization. The two arms of the MZI are designed as width-asymmetric structures to make the sensor more sensitive to the measured material. The asymmetric MZI sensing structure has high RI sensitivity and compact structure, which provides a feasible scheme for biochemical sensing.

1. INTRODUCTION

Biochemical testing is an important process in many applications in healthcare, pharmaceuticals, environmental monitoring, homeland defense, etc. [1]. Integrated label-free optical sensors are a promising choice because they have many unique advantages in biochemical detection, including high refractive index (RI) sensitivity, wide dynamic range, low cost, as well as low detection limits [2, 3]. In addition, they can be integrated with other micro-nano devices and placed in harsh environments. These advantages make integrated label-free optical sensors a strong candidate for on-chip laboratory technology.

Over the past few decades, integrated label-free optical sensors have been extensively studied, such as micro-ring resonator sensors [4–6], MZI sensors [7, 8], Fabry-Pero resonator sensors [9], surface plasmon sensors [10–12], slot waveguide sensors [13], and grating sensors [14]. The MZI structure sensor is one of the well-known label-free optical sensing devices, which has the advantages of high refractive index sensitivity, strong anti-interference ability, and high detection efficiency [15, 16], so we chose the MZI structure design sensor and then observe the wavelength offset of the decay peaks in the transmission spectrum.

Due to the vibrational transition of molecules, the MIR spectral region has many unique characteristics, and it is a research hotspot in many fields, such as safety, medical treatment [17], and environmental monitoring [18, 19]. At the same time, the MIR spectral region shows its potential in many applications, such as optical wireless communication and biological and chemical sensing [20], to reduce transmission loss and improve sensitivity [15]. On the other hand, the MIR spectral region is of great importance in optical detection [21]. This wavelength range contains many chemical and

Received 31 March 2022, Accepted 17 June 2022, Scheduled 13 July 2022

* Corresponding author: Tao Ma (matao@htu.edu.cn).

[1] College of Electronic and Electrical Engineering, Henan Normal University, Xinxiang 453007, China. [2] School of Physics, Henan Normal University, Xinxiang 453007, China. [3] Henan Key Laboratory of Optoelectronic Sensing Integrated Application, Xinxiang 453007, China.

biomolecular absorption fingerprints [15]. So it is obvious that the changes in the refractive index of the matter are to be measured in this wavelength range, where studying MZI refractive index sensing will achieve higher sensitivity and higher resolution.

With the increasing application of the MIR, many materials are used to make MIR sensors, such as silicon (Si) [22], germanium (Ge) [23], and various polymers [24]. Gallium arsenide (GaAs) with a wide transparency range (0.9–17 μm) is a new material used in various electronic and optoelectronic devices [25], compared to Si, SiO_2, polymer, and Ge. In addition, GaAs has heat resistance, radiation resistance, and sensitivity to the magnetic field. In particular, GaAs are considered to be a promising material for the MIR optical devices due to their high nonlinear susceptibility, low absorption, high laser damage threshold, and high thermal conductivity, as well as mature material technology [26].

In this paper, we conduct a preliminary study of the effective refractive index (n_{eff}) characteristics and the waveguide sensitivity (S_{wg}) characteristics of suspended GaAs waveguides. The height (h) and width (w) of the core-layer GaAs waveguide are optimized to obtain a relationship diagram of S_{wg} changing with h and w. We select a suitable suspension GaAs waveguide to design the MZI RI sensor with an operating wavelength of 5 μm. The transmission spectroscopy and sensing performance of the MZI sensor is simulated using the finite element method(FEM). The sensing performance of the MZI sensor on the chemical gas and NaCl solution is studied, and the relationship between the sensing length (L) and refractive index sensitivity (S) is discussed. The quality factor (Q) and detection limit (LOD) of the sensor are estimated.

2. PROPERTY OF SUSPENDED GAAS WAVEGUIDE

2.1. Schematic of GaAs Waveguide

Figure 1(a) shows a schematic cross-sectional diagram of the suspended GaAs waveguide. The waveguide structure is symmetrical, and the production process is simple. The width of the waveguide cladding is $w1 = 6\,\mu m$, and the height is $h1 = 5\,\mu m$. GaAs suspended core layer is covered with air coating, and its original width of $w = 0.7\,\mu m$ and $h = 0.5\,\mu m$. The distance between the core layer and the substrate is $gap = 1\,\mu m$. The waveguide substrate is silica (SiO_2) with a height of $h2 = 1.5\,\mu m$, the same width as the waveguide cladding. In the simulation work, the indices of SiO_2 and GaAs were 1.45 and 3.3, respectively, while the air cladding was 1 and had a working wavelength of 5 μm. Fig. 1(b) and Fig. 1(c) are the TE mode and TM mode of the suspended GaAs waveguide core layer at $w = 1.3\,\mu m$ and $h = 2\,\mu m$, respectively.

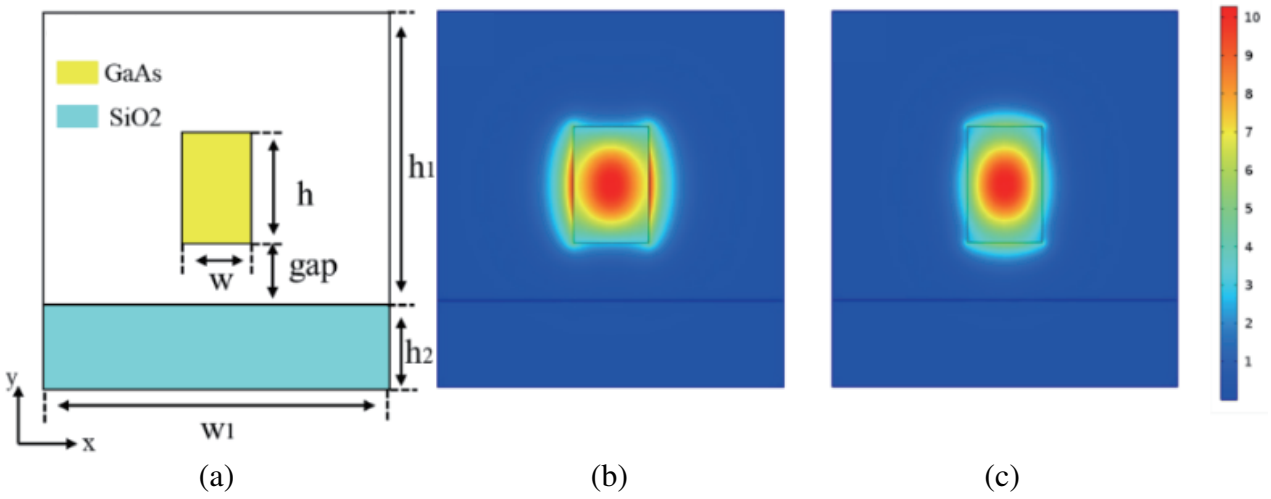

Figure 1. (a) Cross-section of the suspended waveguide. (b) Waveguide core layer TE mode. (c) Waveguide core layer TM mode.

2.2. Characters of Effective Refractive Index

In optical waveguide theory, the effective refractive index (n_{eff}) is the basic physical parameter of the waveguide [27]. n_{eff} mainly depends on the waveguide parameters, i.e., wavelength (λ), w, h, and cladding refractive index (n_{clad}). We set different heights and widths for the core layer of the proposed suspension waveguide structure and studied the effect of the change of core height and width on the effective refractive index. As shown in Fig. 2, Fig. 2(a) and Fig. 2(b) show the change of the effective refractive index with the core layer height and core layer width in the TE mode and TM mode, respectively. As can be seen from Fig. 2, n_{eff} increases with the increase of w at the same height, and n_{eff} increases with the increase of h at the same width. In addition, the increase in the effective refractive index (Δn_{eff}) gradually decreases with the increase of h.

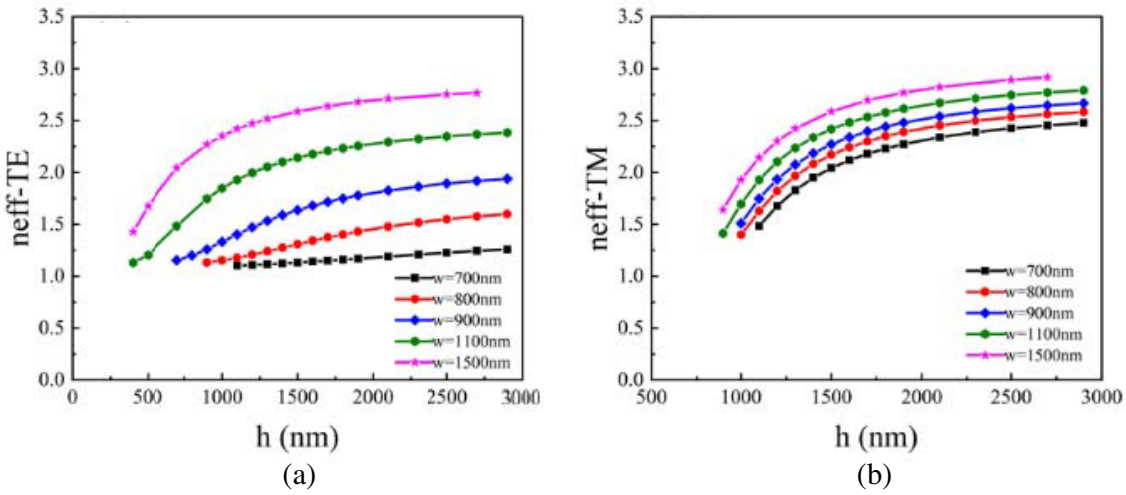

Figure 2. The n_{eff} changes with h and w in TE mode (a), and for TM mode (b).

2.3. Characters of Waveguide Sensitivity

Most optical waveguide RI sensors work based on the fading field, whose light energy is not completely limited to the waveguide core layer, and a small amount of energy is transmitted in the substrate and external environment, which is called fading field. Fading field is sensitive to changes in the external environment, and the sensing target can interact with the light through the fading field, thus causing changes in the optical properties of the device [28]. We can qualitatively analyze the sensing targets by detecting the changes in these optical properties.

Figure 3 is a diagram of S_{wg} with h and w. Fig. 3(a) and Fig. 3(b) show the relationship between TE and TM, respectively. As can be seen from Fig. 3, S_{wg} shows a gradually decreasing trend with the increasing core layer area in both the TE mode and TM mode. This indicates that the core layer area also increases with the core layer width and height, while the binding capacity of the core layer to the light field is also larger. So the fading field outside the core layer decreases, and S_{wg} decreases according to the fading field theory.

3. MZI DESIGN AND ANALYSIS

For MZI sensors, one arm must have a high S_{wg} (sensitivity arm), and the other arm must have a low S_{wg} (or better zero sensitivity) (reference arm) [15, 28]. It is seen from Fig. 3 that the suspended waveguide has a greater S_{wg} in the TE mode, so we chose the TE mode for the calculation. Our chosen waveguide core layer size of the sensitive arm of the MZI was $w4 = 700\,\text{nm}$ and $h = 2100\,\text{nm}$. For the reference arm of the MZI, we need a larger width to reduce the S_{wg} to almost zero. We chose the reference arm waveguide layer size of the MZI as $w3 = 1500\,\text{nm}$ and $h = 2100\,\text{nm}$. The core layer

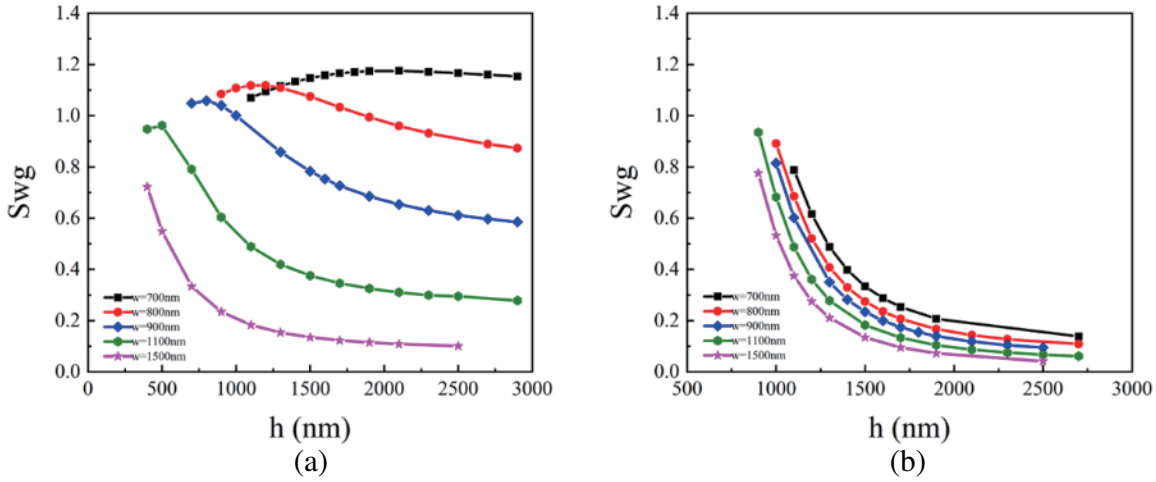

Figure 3. (a) Waveguide sensitivity dependence of the TE mode and (b) waveguide sensitivity dependence of the TM mode on waveguide height (h) and width (w) at $\lambda = 5\,\mu$m.

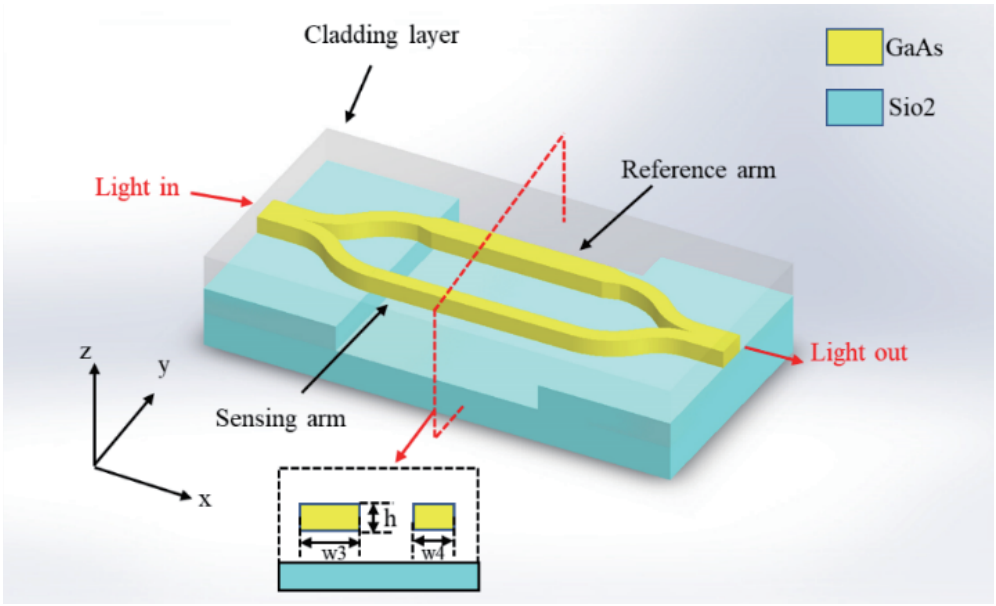

Figure 4. Schematic representation of the 3D and double-arm cross-sections of the MZI.

height is consistent to facilitate the use of plane manufacturing techniques. For the TM mode to reduce the S_{wg} from high to low value, we need to change the waveguide core layer height rather than its width. Fig. 4 shows our three-dimensional (3D) schematic and two-arm cross-section of our MZI sensor designed using a suspended GaAs waveguide.

Our proposed MZI sensing structure has different two-arm widths, so the vanishing fields of the two arms of the MZI are different, and the waveguide sensitivities of the two arms are also different, as shown in Fig. 3. When the RI of the MZI sensor cladding changes, the effective RI of the reference and sensitive arms will also change. In our proposed sensing structure, where both arms of the MZI are exposed to the analyte, the width of both arms is asymmetric, and the width of the reference arm is greater than that of the sensing arm. The light field of the sensing arm interacts with the analyte better than the reference arm. After the light field passes through the sensing arm, the light path changes

with the refractive index of the analyte, which leads to the phase difference between the two arms. Interference stripes are formed in the transmission spectrum. The transmission spectrum appears to redshift as the refractive index of the analyte changes. We can obtain the offset of the wavelength by using the readout system [24].

For the common MZI structures, the output light intensities can be expressed as [27, 29–31]:

$$I = I_1 + I_2 + \sqrt{I_1 I_2}\cos(\Delta\varphi) \tag{1}$$

where I is the output intensity; I_1 and I_2 are the optical intensity propagating along with the sensitive and reference arms, respectively; and $\Delta\varphi$ is the phase difference between the two beams. The phase difference is:

$$\Delta\varphi = \frac{2\pi(n_1 - n_2)L}{\lambda} \tag{2}$$

where L is the sensing length; λ is the incident wavelength; n_1 and n_2 are the effective refractive indices of the sensitive and reference arms. When the phase difference meets the conditions:

$$\Delta\varphi = 2m\pi \tag{3}$$

where m is the order of the MZI. The attenuation peak wavelength λ_m can be expressed as:

$$\lambda_m = \frac{(n_1 - n_2)L}{m} \tag{4}$$

A suspended waveguide-based MZI sensor performs biochemical sensing in an optical waveguide manner. The light field of the suspended waveguide interacts with the surrounding analytes and can induce a change in the effective RI of the MZI [15]. Thus the attenuation peak wavelength is movable [24]. Finally, we can obtain the wavelength offset through the readout system. RI sensitivity is one of the main evaluation indicators for sensing based on the decay peak wavelength offset. Here we intuitively define the refractive index sensitivity as [32]:

$$s = \frac{\Delta\lambda_m}{\Delta n_{clad}} \tag{5}$$

To evaluate the performance of our proposed sensor, we introduce the quality factor (Q) and the limit of detection (LOD). Q is defined as the ratio of the resonance wavelength and the full width half maximum(FEHM) to the transmission spectrum:

$$Q = \frac{\lambda_m}{\mathrm{FWHM}} \tag{6}$$

The limit of detection is defined as:

$$LOD = \frac{\lambda_m}{S \cdot Q} \tag{7}$$

4. THE SIMULATION RESULTS

The FEM is widely used to simulate the resonator electromagnetic behavior in various photonic devices due to the accurate and fast simulations of light interaction with nanostructures [32]. The FEM was therefore used to simulate the performance of the MZI. The calculation was performed in the wave beam envelope, and the boundary pattern analysis was used to calculate the pattern of the port. The regions are closed using the scattering boundary conditions.

Figure 5 shows the top view of our proposed MZI and a light-field transport diagram made with a suspended GaAs waveguide structure. As can be seen from Fig. 5(a), the MZI consists of an input direct waveguide, two Y-type branches, two arms of equal length but different widths and an output direct waveguide. The reference arm is transitioned by narrow width with a gradually tapered waveguide to reduce loss. Because the widths of the MZI arms are different, the transmission intensities of light in the two arms are also different, as shown in Fig. 5(b).

Figure 6 shows the transmission spectra of the MZI of different sensing lengths. Fig. 6(a) is a transmission spectrum of $L = 10\,\mu\mathrm{m}$, with approximately 10 decay peaks in the wavelength range of $4.5\,\mu\mathrm{m}$–$5.5\,\mu\mathrm{m}$. The decay peaks in the MZI transmission spectrum at $L = 23\,\mu\mathrm{m}$ are about 11 as

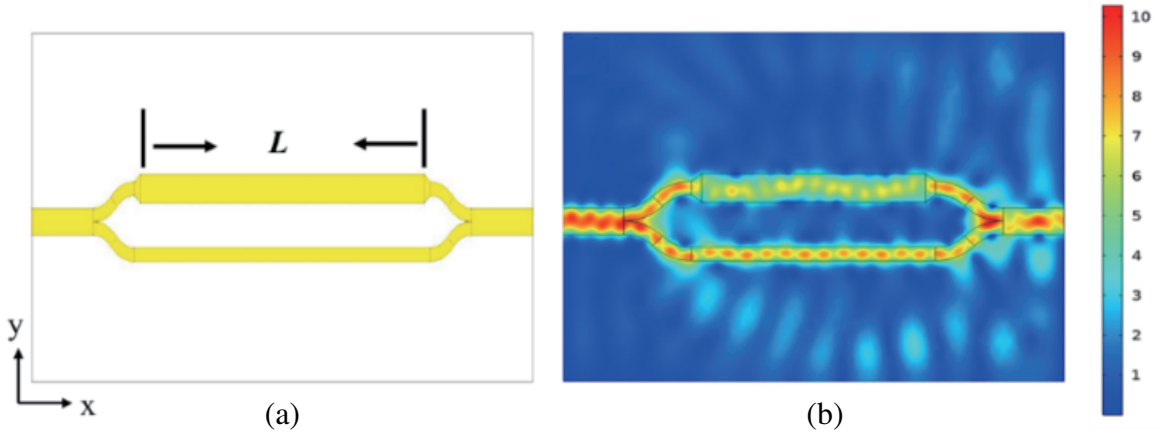

Figure 5. (a) Top view of the MZI. (b) MZI light-field transport diagram.

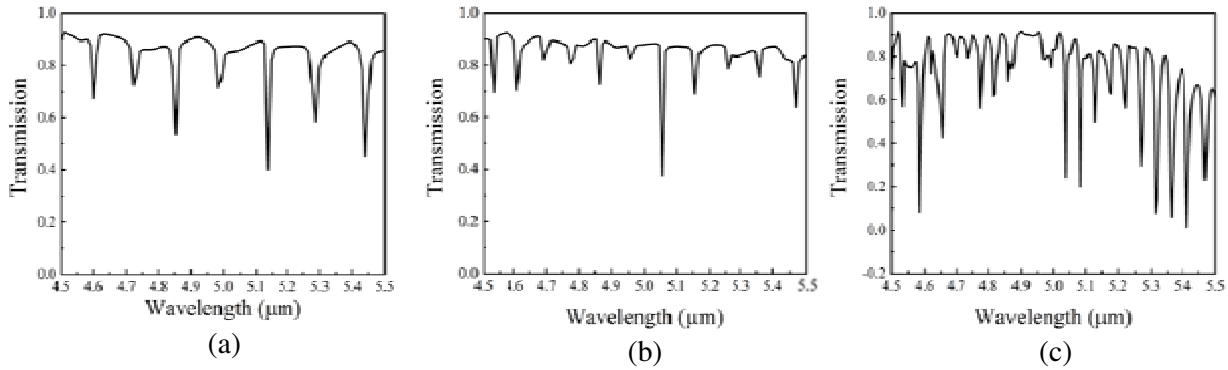

Figure 6. MZI transmitted spectrum (a) $L = 10\,\mu m$, (b) $L = 23\,\mu m$, (c) $L = 90\,\mu m$.

shown in Fig. 6(b). The decay peaks in the MZI transmission spectrum at $L = 90\,\mu m$ also significantly increase the interference stripes of the transmission spectrum.

Comparing Fig. 6(a), Fig. 6(b), and Fig. 6(c), the MZI of longer sensing length shows more interference stripes in the spectrum. The reason may be that the longer sensing length leads to larger phase differences resulting in shorter interference periods [30]. The simulation work results show good agreement with the relationship between the phase difference and the sensing length of the MZI, as shown in equation (2).

The sensing properties of the MZI are achieved by changing the n_{clad}, namely, changes in the peripheral RI. To perform the bulk biochemical sensing, we chose sodium chloride (NaCl) and chemical gas as samples. Nacl and a chemical gas at different aqueous concentrations are listed in Table 1.

Table 1. Average refractive indices of the samples (at temperature of 20°C).

Sample	Concentration %	n_{avr}
Pure water		1.3330
Sodium chloride	$0.5 \sim 15$	1.3592
Chemical gases		$1.00 \sim 1.03$

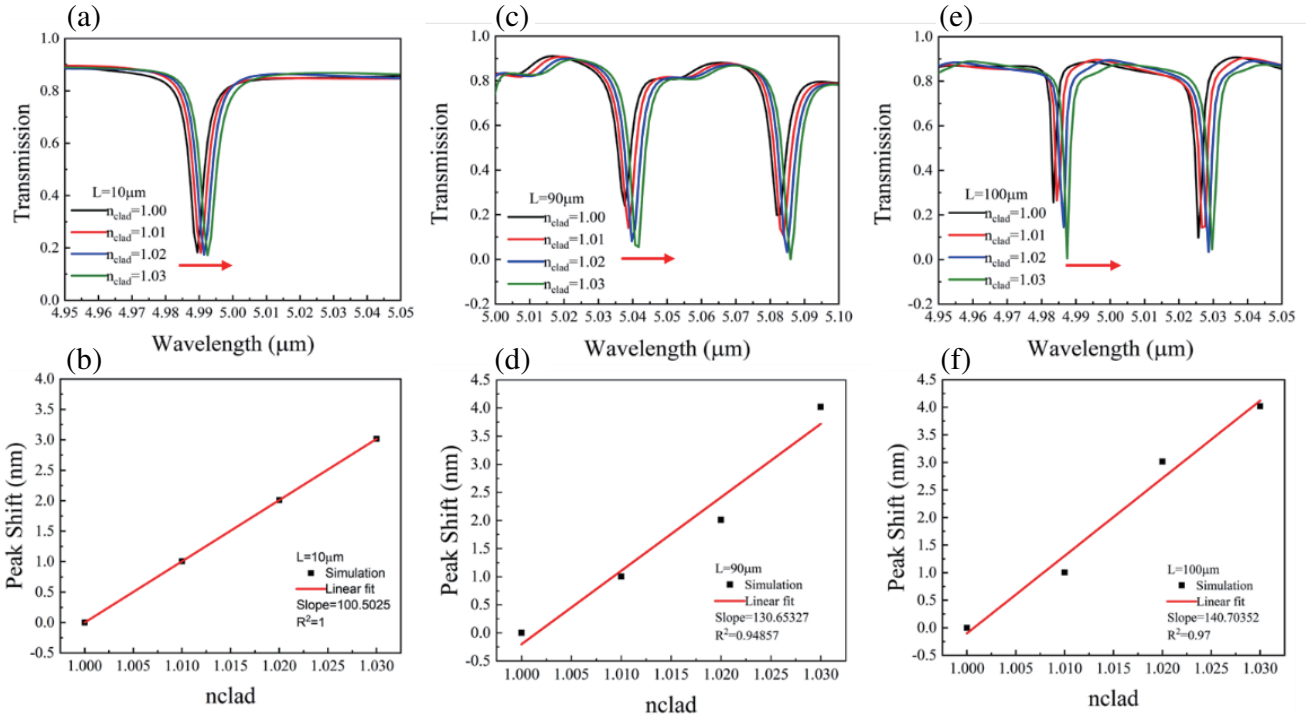

Figure 7. Transmission spectrum of the MZI at different sensing length, (a) $L = 10\,\mu m$, (c) $L = 90\,\mu m$, (e) $L = 100\,\mu m$, (b), (d) and (f) simulation results and linear fitting.

Figures 7(a), 7(c), and 7(e) are the transmission spectra of a chemical gas ($n_{clad} = 1.00 \sim 1.03$) at an MZI sensing length of 10 μm, 90 μm, and 100 μm, respectively. Linear fitting of the simulation results was introduced to discuss the RI sensitivity and linear fitting as shown in Fig. 7(b), Fig. 7(d), and Fig. 7(f). We can learn from Fig. 7 that the transmission spectrum moves in the direction of the wavelength, namely the transmission spectrum shows a red shift [24]. The decay peak of the transmission spectrum moves from 4.989 μm to 4.992 μm in Fig. 7 (a). The decay peak of the transmission spectrum moves from 5.0377 μm to 5.0417 μm in Fig. 7(c). The decay peak of the transmission spectrum in Fig. 7(e) moves from 4.9834 μm to 4.9874 μm. In addition, the slope of the linear fitting (s) also increases as the length of the MZI sensing increases, indicating that a higher sensitivity of RI can be achieved at a longer sensing length. The sensitivity of RI $S = 140.70352\,nm/RIU$ when $L = 100\,\mu m$.

To explore the sensing properties of MZI on the liquid RI change, we changed the value range of n_{clad} from 1.333 to 1.3592. This range is the RI of different concentrations of NaCl solutions. Fig. 8 shows the transmission spectra of the MZI at different sensing lengths as well as the linear fit of the simulation results.

As can be seen from Fig. 8, as n_{clad} increases, the transmission spectra at different sensing lengths appear at red shift, namely, the transmission spectrum moves to the direction of the wavelength increase. The peak of the decay in the transmission spectrum moves from 4.912 μm to 4.917 μm in Fig. 8(a). The peak of the transmission spectral decay in Fig. 8(c) moves from 4.884 μm to 4.890 μm. The transmission spectral decay peak in Fig. 8(e) moves from 4.842 μm to 4.865 μm.

As seen from the linear fitting of Figs. 8(b), (d), and (f) simulation results, the longer sensing length can obtain a better fit and higher RI sensitivity. $S = 854.50788\,nm/RIU$ when the sensing length is $L = 48\,\mu m$. We can see from Fig. 8 that the RI sensitivity of MZI is greater than that of MZI when the envelope is a chemical gas. This shows that MZI senses Nacl solution better than chemical gas. A comparison of Fig. 7 and Fig. 8 shows that a higher RI sensitivity and a longer sensing length are required when the coating is a chemical gas. In addition, the size of the sensor should also be increased, which is not conducive to device integration. However, when the coating is a NaCl solution, the sensing length of the MZI compared to the chemical gas is not very long to achieve higher RI sensitivity, making

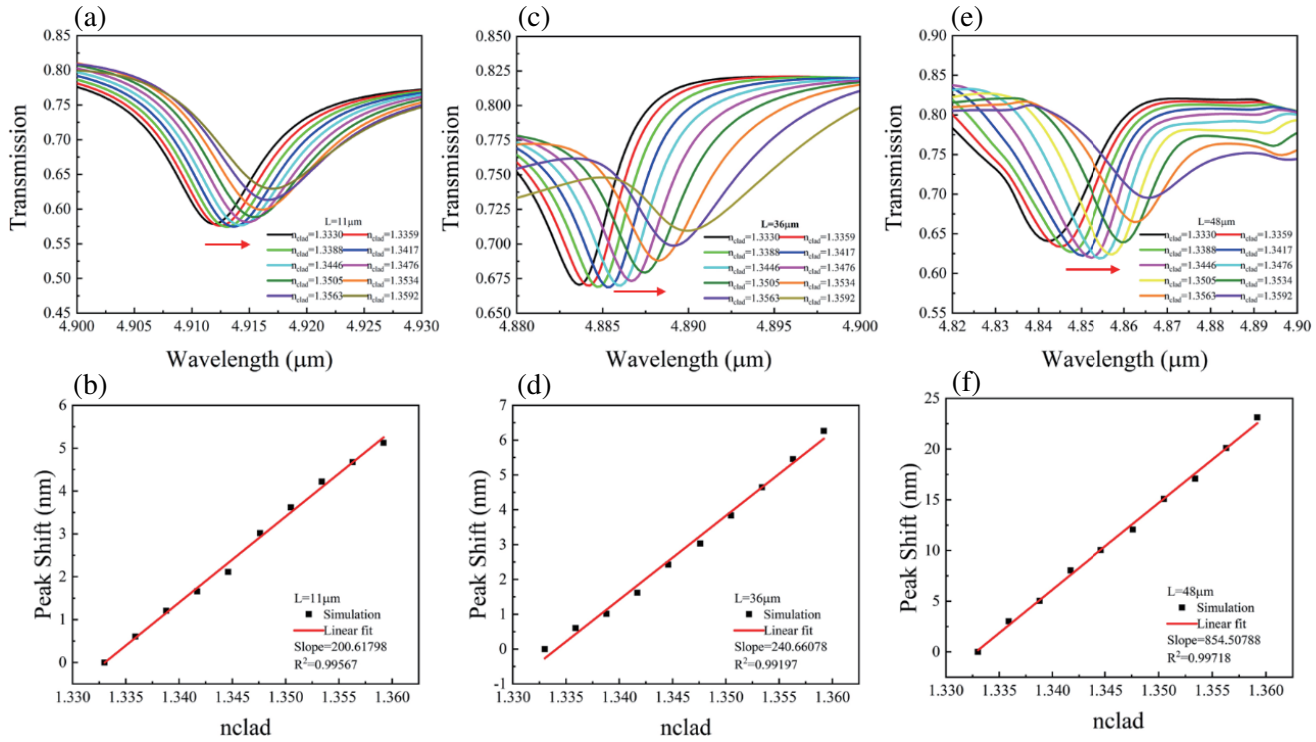

Figure 8. Transmission spectrum of the MZI at a sensing length of 11 μm (a), 36 μm (c), and 48 μm (e), respectively. (b), (d) and (f) simulation results and linear fitting.

it possible to make a low-cost and highly integrated Nacl solution RI sensor using our designed MZI.

In Table 2, the performance parameters of the MZI sensors are listed in the different sensing lengths. As shown in Table 2, the optimal sensing length of the MZI sensor when the substance tested is a chemical gas should be $L = 100$ μm, at which the MZI sensor has the largest RI sensitivity, largest Q value, and minimum detection limit. When the measured material is a NaCl solution, the optimal sensing lengths of the MZI sensor are 36 μm and 48 μm. Because the maximum Q value of the MZI sensor was found at $L = 36$ μm and the maximum RI sensitivity of the MZI sensor at $L = 48$ μm, the detection limit difference in the upper two cases was small and smaller than the detection limit of the MZI sensor at $L = 11$ μm.

Table 2. Performance parameters of the MZI sensor at different sensing lengths (L).

Substances to be testd	Chemical gases			Sodium chloride		
L (μm)	10	90	100	11	36	48
S (nm/RIU)	100.5025	130.62327	140.70352	200.61798	240.66078	854.50788
Q	943	1214	3078.5	548.8	892.4	208.2
LOD (RIU)	0.05263103	0.03176	0.011505	0.044607	0.022737	0.027215

In Table 3, a comparison of the proposed sensors has been shown with some recent works in the last few years. Our proposed sensor structure has a higher RI sensitivity, and the maximum RI sensitivity can reach 854.5 nm/RIU.

Table 3. Comparison of the proposed sensor with the other structures.

Ref.	Year	RI Sensitivity (nm/RIU)
Yongjiao Wen et al. [33]	**2019**	**500**
Souvik Ghosh et al. [34]	**2019**	**437.3**
La Xiang et al. [35]	**2020**	**494**
Bahram Azizi et al.[36]	**2021**	**600**
Hongling Zhang et al. [37]	**2021**	**847**
Our proposed sensors	**2022**	**854.5**

5. CONCLUSIONS

In summary, a mid-infrared asymmetric MZI made from suspended GaAs waveguides is proposed, and its mode propagation properties and biochemical sensing performances are investigated. The design of the suspension structure facilitates the interaction between the measured material and the vanishing field. The asymmetric design allows the sensor to respond more quickly to the measured material. The characteristics of effective mode RI and S_{wg} properties of the suspended GaAs waveguides in the mid-infrared range are studied. The RI sensitivity of the asymmetric MZI is optimized by scanning the length of the sensing arm. The asymmetric MZI sensing structure with high RI sensitivity and compact structure has great application prospects in the mid-infrared biochemical sensing, point-of-care diagnostics, and healthcare applications.

6. FUNDING

Natural National Science Foundation of China (NSFC) (62075057).

REFERENCES

1. Zhang, D., H. Wei, and S. Krishnaswamy, "3D printing optofluidic Mach-Zehnder interferometer on a fiber tip for refractive index sensing," *IEEE Photonics Technology Letters*, Vol. 31, No. 21, 1725–1728, 2019.
2. Dziekan, Z., E. Pitula, N. Kwietniewski, B. Stonio, M. Janik, T. Śmiarowski, M. Koba, P. Parzuchowski, J. Niedziĺka-J"onsson, and M. Smietana, "Performance of nanoimprinted and nanocoated optical label-free biosensor — nanocoating properties perspective," *Optics and Lasers in Engineering*, Vol. 153, 2022.
3. Berneschi, S., F. Bettazzi, A. Giannetti, F. Baldini, G. Nunzi Conti, S. Pelli, and I. Palchetti, "Optical whispering gallery mode resonators for label-free detection of water contaminants," *TrAC Trends in Analytical Chemistry*, Vol. 126, 2020.
4. Javanshir, S., A. Pourziad, and S. Nikmehr, "Optical temperature sensor with micro ring resonator and graphene to reach high sensitivity," *Optik*, Vol. 180, 442–446, 2019.
5. Ajad, A. K., M. J. Islam, M. R. Kaysir, and J. Atai, "Highly sensitive bio sensor based on WGM ring resonator for hemoglobin detection in blood samples," *Optik*, Vol. 226, 2021.
6. Lin, Y., W. Qian, H. Li, H. Ma, and Z. Jin, "Resonant micro optic gyroscope equipped with multi-turn waveguide ring resonator," *Optics Communications*, Vol. 491, 2021.
7. Roldán-Varona, P., D. Pallarés-Aldeiturriaga, L. Rodríguez-Cobo, and J. M. López-Higuera, "All-in-fiber multiscan Mach-Zehnder interferometer assisted by core FBG for simultaneous multi-parameter sensing," *Optics & Laser Technology*, Vol. 132, 2020.
8. Lotfi, F., N. Sang-Nourpour, and R. Kheradmand, "High-sensitive plasmonic sensor based on Mach-Zehnder interferometer," *Optics & Laser Technology*, Vol. 137, 2021.

9. Yuan, G., L. Gao, Y. Chen, J. Wang, P. Ren, and Z. Wang, "Efficient optical biochemical sensor with slotted Bragg-grating-based Fabry-Perot resonator structure in silicon-on-insulator platform," *Optical and Quantum Electronics*, Vol. 47, No. 2, 247–255, 2014.
10. Jiang, Y., C. Shi, and J. Wang, "A hybrid plasmonic terahertz waveguide with ridge structure base on Bulk-Dirac-semimetal," *Optics Communications*, Vol. 475, 2020.
11. Chang, Y. and Y. Jiang, "Highly sensitive plasmonic sensor based on fano resonance from silver nanoparticle heterodimer array on a thin silver film," *Plasmonics*, Vol. 9, No. 3, 499–505, 2013.
12. Al Mahmud, R., M. O. Faruque, and R. H. Sagor, "A highly sensitive plasmonic refractive index sensor based on triangular resonator," *Optics Communications*, Vol. 483, 2021.
13. Wang, Y., W. Chen, P. Wang, S. Dai, J. Li, Y. Li, Q. Fu, T. Dai, H. Yu, and J. Yang, "Ultra-high-power-confinement-factor integrated mid-infrared gas sensor based on the suspended slot chalcogenide glass waveguide," *Sensors and Actuators B: Chemical*, Vol. 347, 2021.
14. Heinsalu, S., Y. Isogai, A. Kawano, Y. Matsushima, H. Ishikawa, and K. Utaka, "Proposal and analysis of ultra-high amplitude-sensitive refractive index sensor by thick silicon multi-slot sub-wavelength Bragg grating waveguide," *Optics Communications*, Vol. 505, 2022.
15. El Shamy, R. S., M. A. Swillam, and D. A. Khalil, "Mid infrared integrated MZI gas sensor using suspended silicon waveguide," *Journal of Lightwave Technology*, Vol. 37, No. 17, 4394–4400, 2019.
16. Hodgkinson, J. and R. P. Tatam, "Optical gas sensing: a review," *Measurement Science and Technology*, Vol. 24, No. 1, 2013.
17. Chang, Y.-C., P. Wgli, V. Paeder, A. Homsy, L. Hvozdara, P. van der Wal, J. Di Francesco, N. F. de Rooijb, and H. P. Herziga, "Cocaine detection by a mid-infrared waveguide integrated with a microfluidic chip," *Lab on a Chip*, Vol. 12, No. 17, 2012.
18. Tu, Z., X. Guan, D. Chen, H. Hu, X. Wang, and S. Gao, "2 µm mid-infrared silicon-rich silicon nitride/silicon hybrid nonlinear waveguides," *Optics Communications*, Vol. 481, 2021.
19. Wang, F., Y. Chen, C. Li, T. Ma, X. Wang, K. Yu, and L. Li, "Ultracompact and broadband mid-infrared polarization beam splitter based on an asymmetric directional coupler consisting of GaAs-CaF_2 hybrid plasmonic waveguide and GaAs nanowire," *Optics Communications*, Vol. 502, 2022.
20. Yu, C., A. Ganjoo, H. Jain, C. G. Pantano, and J. Irudayaraj, "Mid-IR biosensor: Detection and fingerprinting of pathogens on gold island functionalized chalcogenide films," *Analytical Chemistry*, Vol. 78, 2500–2506, 2006.
21. Zouache, T. and A. Hocini, "Mid-infrared micro-displacement measurement with a bidimensional silicon photonic crystal," *Progress In Electromagnetics Research Letters*, Vol. 91, 77–83, 2020.
22. Singh, V., P. T. Lin, N. Patel, H. Lin, L. Li, Y. Zou, F. Deng, C. Ni, and J. Hu, "Mid-infrared materials and devices on a Si platform for optical sensing," *Sci. Technol. Adv. Mater.*, Vol. 15, No. 1, Feb. 2014.
23. Lee, J.-M., M. K. Kim, and W.-Y. Choi, "Series resistance influence on performance of waveguide-type germanium photodetectors on silicon," *Chinese Optics Letters*, Vol. 15, No. 10, 2017.
24. Jiang, L., J. Wu, K. Chen, Y. Zheng, G. Deng, X. Zhang, Z. Li, and K. S. Chiang, "Polymer waveguide Mach-Zehnder interferometer coated with dipolar polycarbonate for on-chip nitroaromatics detection," *Sensors and Actuators B: Chemical*, Vol. 305, 2020.
25. Wang, J., A. Santamato, P. Jiang, D. Bonneau, E. Engin, J. W. Silverstone, M. Lermer, J. Beetz, M. Kamp, S. Höfling, M. G. Tanner, C. M. Natarajan, R. H. Hadfield, S. N. Dorenbos, V. Zwiller, J. L. O'Brien, M. G. Thompson, "Gallium arsenide (GaAs) quantum photonic waveguide circuits," *Optics Communications*, Vol. 327, 49–55, 2014.
26. Yao, F., M. Yang, Y. Chen, X. Zhou, and L. Wang, "Firstprinciples calculations of the electronic, and optical properties of a GaAs/AlAs van der Waals heterostructure," *Chemical Physics Letters*, Vol. 765, 2021.
27. Chen, C., X. Hou, and J. Si, "Theoretical design of an integrated optical sensor for a standard immunoassay," *IEEE Sensors Journal*, Vol. 18, No. 13, 5368–5375, 2018.

28. Fan, X., I. M. White, S. I. Shopova, H. Zhu, J. D. Suter, and Y. Sun, "Sensitive optical biosensors for unlabeled targets: a review," *Anal. Chim. Acta.*, Vol. 620, No. 1–2, 8–26, Jul. 14, 2008.
29. Hong, J., J. S. Choi, G. Han, J. K. Kang, C. M. Kim, T. S. Kim, and D. S. Yoon, "A Mach-Zehnder interferometer based on silicon oxides for biosensor applications," *Anal. Chim. Acta.*, Vol. 573–574, 97–103, Jul. 28, 2006.
30. Zhang, D., L. Men, and Q. Chen, "Femtosecond laser microfabricated optofluidic Mach-Zehnder interferometer for refractive index sensing," *IEEE Journal of Quantum Electronics*, Vol. 54, No. 6, 1–7, 2018.
31. Zhang, D., L. Men, and Q. Chen, "Waveguide Mach-Zehnder interferometer for temperature and concentration sensing," *IEEE Journal of Selected Topics in Quantum Electronics*, Vol. 27, No. 4, 1–7, 2021.
32. Ma, T., L. Sun, J. Yuan, X. Sang, B. Yan, K. Wang, and C. Yu, "Integrated label-free optical biochemical sensor with a large measurement range based on an angular grating-microring resonator," *Appl. Opt.*, Vol. 55, No. 18, 4784–4790, Jun. 20, 2016.
33. Wen, Y., Y. Sun, C. Deng, L. Huang, G. Hu, B. Yun, R. Zhang, and Y. Cui, "High sensitivity and FOM refractive index sensing based on Fano resonance in all-grating racetrack resonators," *Optics Communications*, Vol. 446, 141–146, 2019.
34. Ghosh, S. and B. M. A. Rahman, "Design of on-chip hybrid plasmonic Mach-Zehnder interferometer for temperature and concentration detection of chemical solution," *Sensors and Actuators B: Chemical*, Vol. 279, 490–502, 2019.
35. Xiang, L. and L. Huang, "High-sensitivity complex refractive index sensor by designing a slot-waveguide side-coupled Fano resonant cavity," *Optics Communications*, Vol. 475, 2020.
36. Azizi, B., M. A. G. Shabankareh, and A. Farmani, "Simulation of a refractive index sensor based on the Vernier effect and a cascaded PANDA and Mach-Zehnder interferometer," *Journal of Computational Electronics*, Vol. 20, No. 4, 1599–1610, 2021.
37. Zhang, H., B. Cong, F. Zhang, Y. Qi, and T. Hu, "Simultaneous measurement of refractive index and temperature by Mach-Zehnder cascaded with FBG sensor based on multi-core microfiber," *Optics Communications*, Vol. 493, 2021.